

Article

Numerical and Experimental Study on Hot Forming by Partition Cooling of 38MnB5Nb

Xiao Liang ¹, Xianjun Li ¹, Decheng Wang ¹, Xiyue Lin ¹, Ping Luo ¹, Zhunli Tan ², Yong Song ³, Yu Tian ², Junqing Hou ¹, Chao Jiang ¹, Yi Bian ^{1,4} and Huasheng Xie ^{1,*}

- ¹ China Academy of Machinery Science and Technology, Beijing 100048, China; liangxiao@brimet.ac.cn (X.L.); imlixj@163.com (X.L.); wangdc@cam.com.cn (D.W.); lxy950703@163.com (X.L.); 13121304@bjtu.edu.cn (P.L.); hjqofking@163.com (J.H.); jiangchao@brimet.ac.cn (C.J.); bianyi@brimet.ac.cn (Y.B.)
- ² School of Mechanical, Electronic and Control Engineering, Beijing Jiaotong University, Beijing 100044, China; tzli@bjtu.edu.cn (Z.T.); 17121354@bjtu.edu.cn (Y.T.)
- ³ Institute of Engineering Technology, University of Science and Technology Beijing, Beijing 100083, China; songyong@ustb.edu.cn
- ⁴ School of Engineering Science, University of Science and Technology of China, Hefei 230027, China
- * Correspondence: xiehs@chinasrif.com; Tel.: +86-188-8887-1011

Abstract: Tailored properties hot forming of 38MnB5Nb by partition cooling can be configured on-demand. A gradient distribution microstructural characteristic can be generated by undertaking an appropriate cooling-tempering process for the regions with different properties requirements before forming. A unified viscoplastic constitutive model coupled with the primary cooling temperature and related material constants is established based on genetic algorithm. Meanwhile, the use of the mixture of jet air and dry ice particles to cool the partition region is essential to achieve different primary cooling temperatures. In this paper, the inverse heat conduction problem is solved to obtain the relationship between the interfacial heat transfer coefficient and different cooling conditions in the partition cooling process. The U-shaped part is taken as an example to simulate the change of temperature, stress-strain, thickness, and spring-back in the process of partition cooling and tailored hot forming properties. The results show that the gradient microstructural characteristic formed by partition cooling has a great influence on the stress field distribution. The maximum stress of 345 MPa can be reached after complete pressure holding in the partition slow cooling tailored properties of the hot forming process. The maximum stress can reach 743 MPa in the partition fast cooling tailored properties of the hot forming process due to the relatively high deformation resistance of the tempered martensite at the bottom center. The maximum residual stress in the two processes after spring-back drops to 305 MPa and 545 MPa, respectively. The spring-back is small under the two processes, with a maximum spring back angle of no more than 1°.

Keywords: hot forming; partition cooling; tailored properties; constitutive model



Citation: Liang, X.; Li, X.; Wang, D.; Lin, X.; Luo, P.; Tan, Z.; Song, Y.; Tian, Y.; Hou, J.; Jiang, C.; et al. Numerical and Experimental Study on Hot Forming by Partition Cooling of 38MnB5Nb. *Metals* **2022**, *12*, 839. <https://doi.org/10.3390/met12050839>

Academic Editor: Koh-ichi Sugimoto

Received: 14 April 2022

Accepted: 10 May 2022

Published: 13 May 2022

Publisher's Note: MDPI stays neutral with regard to jurisdictional claims in published maps and institutional affiliations.



Copyright: © 2022 by the authors. Licensee MDPI, Basel, Switzerland. This article is an open access article distributed under the terms and conditions of the Creative Commons Attribution (CC BY) license (<https://creativecommons.org/licenses/by/4.0/>).

1. Introduction

In order to meet the increasing requirements for lightweight, energy-saving and emission reduction of automobiles, and improve crash safety performances, ultra-high-strength steel (UHSS) is used in the manufacture of important structural and safety parts, such as A-pillars, B-pillars, bumpers, anti-collision beam and roof rail. UHSS hot forming technology has the advantages of small forming load and small spring-back, which can make UHSS form a martensite to ensure its ultra-high strength [1,2]. Therefore, hot forming technology is widely used in the production of body-in-white components. Recently, it has been proposed that different mechanical properties should be applied to the same part to achieve better impact energy absorption. Thus, on the basis of the traditional hot forming technology, the tailored properties process of hot forming (TPP) is proposed, which can make specific regions of the part have higher tensile strength and lower ductility to improve

intrusion resistance [3]. Regions that need to improve energy absorption properties have higher ductility [4], whereas, the regions such as trimming and perforation require lower strength [5,6]. At present, the tailored properties of collision structural parts based on the hot forming is mostly realized by welding [7,8], rolling [9], partition heating [10–13], differential cooling [14,15] and annealing [16–19]. Merklein [10] and Nakagawa [1] summarized the ways to realize the TPP.

Tailor-welded blank (TWB) hot forming technology is to connect two or more metal blanks with different properties by welding before forming. Munera et al. [20] tailor-welded the Ductibor 1500P blank with good stability and high ductility after quenching and USIBOR 1500P blank with high quenching strength but poor plasticity to reduce the weight of the body-in-white. Tang et al. [21] established a multi-field coupled numerical model to simulate the hot forming of laser-welded blank and verified the reliability of the model by hot forming experiments of B-pillar stiffener parts. Lamprecht et al. [8] found that the coating layer should be removed before the Al-Si coated UHSS blanks were welded since the mesophase formed by the reaction of Al and Si with the matrix would weaken the mechanical properties of the welding line.

Tailor-rolled blank (TRB) hot forming technology is to apply different thicknesses in different regions on the same material with complex rolling technology to obtain different mechanical properties. Billur et al. [22] designed uncoated and coated blanks with different thicknesses to satisfy the mechanical properties needed by the final product, which are manufactured by flexible rolling process. Lei et al. [23] conducted high-temperature tensile tests at different strain rates using UHSS blanks with different thicknesses and established a high-temperature constitutive relationship of unequal thickness blanks. Hang et al. [24] used forming limit surface (FLS) the influence of thickness to evaluate the formability of the front longitudinal of TRB.

UHSS can be austenitized when heated to above austenite transformation temperature A_{c3} , and then transformed into a high-strength martensite through hot forming. The transformation can be prevented by controlling the temperature of the parts of the blank below A_{c3} , so that its strength is lower, but its plasticity is better. Wilsius et al. [25] placed different regions of the blank in different furnaces with different temperatures to obtain different degrees of austenitization to achieve a gradient distribution of the strength of the parts. Mori et al. [12,26] designed a heating device with shunt resistance. The contact part between the copper electrode and the blank was a low-strength region, and the partition austenitization of the blank was realized by electric heating. Mu et al. [27] analyzed the austenitization mechanism during the heating process and established a dynamic model of austenitization transformation suitable for partition heating, as well as a unified viscoplastic model coupled with the austenite volume fraction through elevated-temperature tensile test.

The part is quenched and cooled uniformly in the traditional hot forming, and the microstructure of the part is martensite. Based on the characteristic of phase transformation when cooling UHSS, partition cooling technology controls the cooling rate in different regions of the part and produces different microstructures in different regions, thereby achieving different strength and toughness distributions. Mori et al. [14] got a non-contact part with the blank during forming by grooving the die. The strength of the non-contact part was low due to the lack of quenching, while the strength of the contacted part was high due to quenching. Feuser et al. [28] established a complete process window to realize the change of mechanical properties by heating the die, which was verified by numerical simulation. Casas et al. [29] designed a block die to obtain different thermal conductivities on different die blocks. In the region of low thermal conductivity, the rate of heat exchange between the blank and the die is low, and the cooling rate is low, resulting in bainite and ferrite/pearlite. However, in the region with high thermal conductivity, a martensitic microstructure is formed due to high heat exchange rate. Kolleck et al. [30] inlaid heat-insulating materials such as stoneware bricks in the die, which are hard to cool due to the

large heat capacity to reduce the temperature difference between the mold and the blank, resulting in low cooling rate.

Tailored tempering technology was proposed by ThyssenKruppTM. The principle is that the parts are partially tempered after the forming of the blank, so that the strength of the partial region is reduced and the plasticity is improved. The methods of tempering include flame heating, electromagnetic induction heating and laser heating. The control of temperature during the tempering process is the key, and the warping deformation of parts during the tempering process should be considered. Zimmermann et al. [31] tempered parts by flame heating. When the maximum tempering temperature was 793 °C, the minimum strength of the parts was 580 MPa, and the size of the transition region was 40 mm~45 mm. Wang et al. [32] used a tailored tempering hot forming to achieve different hardness distributions in different regions, and the elongation in the annealed regions reached 20.6%.

In this paper, TPP, which is different from the five methods mentioned above, is proposed to realize the on-demand customization of the properties of UHSS, help reduce costs, and improve production efficiency. A constitutive model considering the process of heat treatment before forming is also proposed, and the distribution of interfacial heat transfer coefficient in different regions under different cooling states is obtained by calculation. The hot forming of tailored properties of U-shaped parts is simulated by FEM simulation ABAQUS 2020/Explicit software, and the accuracy of the numerical model is verified by hot forming experiments.

2. Tailored Properties Hot Forming

Two TPP are proposed, which are partition slow cooling tailored properties hot forming process (TPP-S) and partition fast cooling tailored properties hot forming process (TPP-F) according to the different cooling rates in soft region. The TPP-S (Figure 1a) requires that blanks to be heated to above the martensite start temperature M_s in the soft regions after fully austenitizing, and the hard regions to be cooled to below the temperature of A_{c3} due to the influence of soft regions cooling (generally no higher than 100 °C). The whole blank is tempered to keep the soft regions below A_{c3} temperature while the hard regions are above temperature A_{c3} before the blank is quenched, after which the microstructure is ferrite and pearlite in the soft regions and martensite in the hard region. The TPP-F (Figure 1b) is different from the TPP-S in the primary cooling section, which requires rapid cooling to below martensite finish temperature M_f in the soft regions to form martensite, and then tempering to form tempered structure (tempered martensite and tempered sorbite). After quenching, the soft regions are tempered structure, and the hard regions are all martensite.

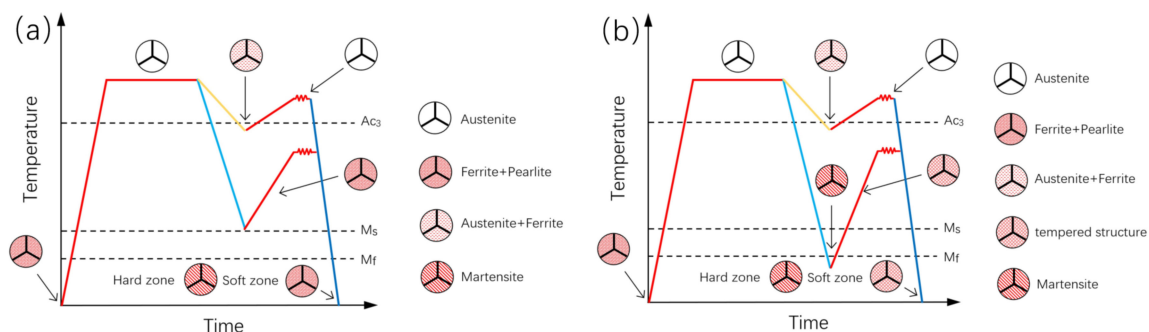


Figure 1. (a) TPP-S; (b) TPP-F. Red lines (heating and isothermal), Yellow lines (slow cooling), blue and dark blue lines (fast cooling).

3. Material and Specimen

In this experiment, the Al-Si coated 38MnB5Nb hot-rolled blank produced by ShougangTM Group was used. The material composition shown in Table 1. All speci-

mens used for the experiment were machined from the same batch of as-delivered steel, which was 2 mm thick, and had a microstructure of about 64% ferrite and 36% pearlite.

Table 1. Chemical compositions of as-received 38MnB5Nb steel (mass%).

Material	C	Si	Mn	Cr	Al	Ti	Mo	Nb	V	B
38MnB5Nb	0.36	0.24	1.39	0.19	0.05	0.05	0.002	0.05	0.05	0.0035

Elevated-temperature tension testing was carried out with a Gleeble 3500c thermo-mechanical simulator (DSI Inc., New York, NY, USA), which was a fully integrated digital closed loop control of thermal and mechanical testing system, combined with independent control of strain and strain rates which were ideally suited to simulate the manufacturing processes, in particular the stress-strain behavior of materials. The elevated-temperature tension testing specimen (geometrical size shown in Figure 2) was taken from the blank, which was cut by wire and polished with sandpaper.

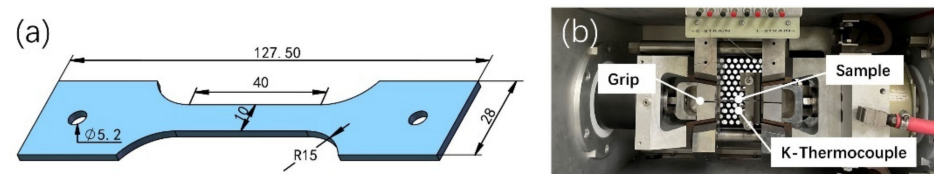


Figure 2. (a) Sketch of the elevated-temperature tension testing specimen (units in mm), (b) Schematic diagram of the elevated-temperature tension test.

In order to analyze the thickness distribution after forming and rebound angle change after spring-back, the MCAx 3D scanner (Nikon Metrology Inc., Brighton, CA, USA), offering a measuring accuracy down to 10 microns, is used to carry out a digital modeling analysis of the blank after TPP-S and TPP-F, as shown in Figure 3.

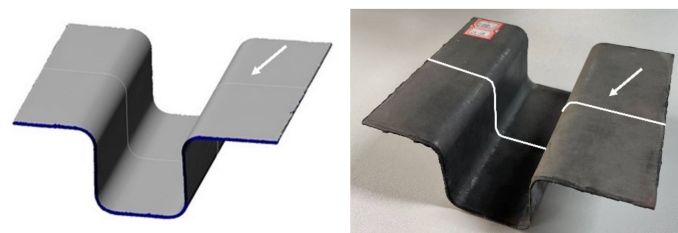


Figure 3. Schematic diagram of experimental the U-shaped part and thickness detection positions. The arrow position is the measurement section.

4. Elevated-Temperature Tension Testing

4.1. Testing Procedure

The experiment includes three groups of tests, as shown in Figure 4. The hot forming of fast cooling and slow cooling in the soft regions were simulated in groups A and B. Firstly, the specimen is heated to 620 °C at a heating rate of 10 °C/s and then heated to 920 °C (above A_{c3}) at a rate of 1.25 °C/s for 30 s for the complete austenitization. This heating method simulates the actual temperature rise of the blank in a standard electric furnace FO810(Yamato Scientific Co.,Ltd., Tokyo, Japan). After complete austenitization, Group A was rapidly cooled at 36 °C/s to 200 °C (lower than M_f) for 5 s, as 36 °C/s was greater than the critical cooling rate of 10 °C/s, which could ensure a higher volume fraction of martensitic microstructure. Then the blank was heated to 550 °C, 650 °C, 750 °C at 18 °C/s, 23 °C/s, 28 °C/s respectively, and held for 5 s at each temperature. Group B was cooled to 450 °C (between A_{c3} and M_s) at 24 °C/s and kept for 5 s. Then the blank

was heated to 550 °C, 650 °C, 750 °C at 5 °C/s, 10 °C/s, 15 °C/s respectively and held for 5 s at each temperature.

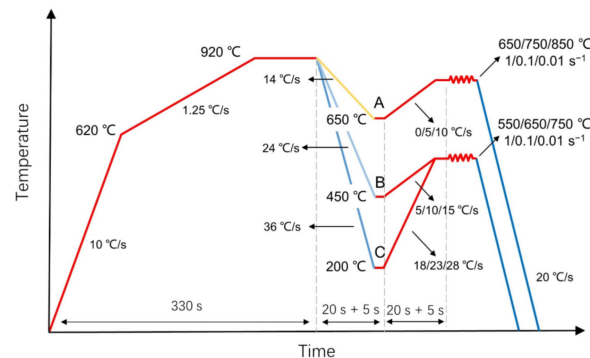


Figure 4. Experiment process of the hot tensile testing (units in mm). Red lines (heating and isothermal), Yellow lines (slow cooling), blue and dark blue lines (fast cooling).

The hot forming of the hard regions was simulated in group C. The heating stages were the same as that of group A and B. After completing austenitization, the material was cooled to 650 °C (lower than A_{c3}) at 14 °C/s and held for 30 s, or cooling to 650 °C for 5 s, heated to 750 °C, 850 °C at 5 °C/s, 10 °C/s held for 5 s at each temperature to ensure uniform temperature distribution, and to obtain a mixed microstructure composed of austenite, ferrite, and pearlite.

Afterward, the specimens of groups were stretched at strain rates of 1 s^{-1} , 0.1 s^{-1} , and 0.01 s^{-1} , and finally cooled to room temperature at a cooling rate of 20 °C/s.

4.2. Flow Behavior

Both the work hardening and dynamic softening processes exist in the high-temperature deformation of 38MnB5Nb. During the deformation process, dislocation multiplication and mutual accumulation lead to work hardening. Dislocation merge and recombine through climbing or cross-slip, and the material undergoes dynamic recovery and softening due to external stress and thermal activation. At the beginning of deformation, the flow stress grows rapidly with the increase of strain, which results in continuous dislocation proliferation. Meanwhile, the interaction between dislocations increases the movement resistance of dislocations. At the same time, due to the small strain and small intracrystalline storage energy, the dynamic softening process is difficult to carry out, while work hardening is dominant at this time. When the stress reaches the peak value, the material enters the steady deformation stage. As the strain is gradually increased, the intracrystalline storage energy gradually increases, and the dynamic softening and strain hardening tend to be balanced. At this time, the speed of dislocation movement is extremely fast, while the hardening and softening are completed almost simultaneously in the process of thermal deformation. When the hardening and softening reach a dynamic equilibrium, the true stress-strain curve of the material tends to be horizontal [33]. The segment of the stress-strain curves exhibiting a precipitous decrease was not the focus of this work, the damage incurred was not taken into account while modeling the constitutive descriptions of 38MnB5Nb, according to a previously published extension method [34], the true stress-strain curves can be extended, groups A, B, and C of 38MnB5Nb at 550 °C, 650 °C, 750 °C and 850 °C are shown in Figure 5.

The primary cooling temperature, deformation temperature, and strain rate have obvious effects on the thermal flow behavior of 38MnB5Nb. It can be seen from Figure 5 that the peak stress decreases with the rise of the deformation temperature at the same strain rate. As shown in Figure 5c, when the primary cooling temperature is 650 °C, under the strain rates of 0.01 s^{-1} , 0.1 s^{-1} , and 1 s^{-1} , the peak stresses at the deformation temperature of 750 °C are 193 MPa, 245 MPa, and 320 MPa, respectively. When the deformation temperature is 850 °C, the peak stresses are 125 MPa, 169 MPa, and 236 MPa, respectively.

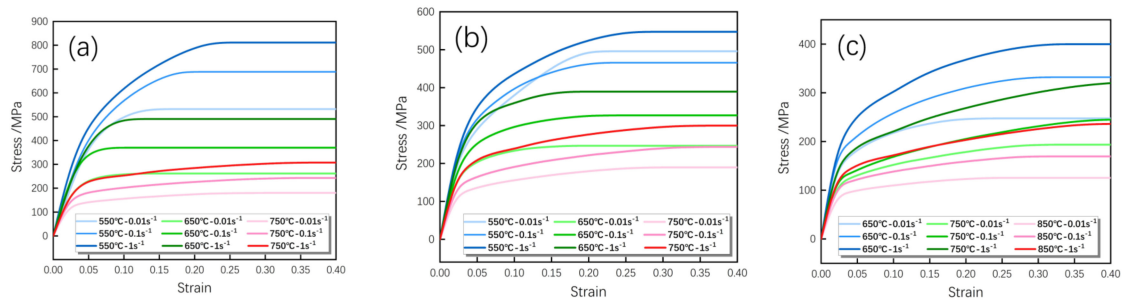


Figure 5. The stress-strain curves. (a) Group A TPP-F; (b) Group B TPP-S; (c) Group C hard regions.

Figure 5a,c indicates that, under a certain deformation temperature, as the strain rate rises, the material does not have enough time for dynamic recovery and recrystallization. Peak stress is greater at high strain rates than at low strain rates, in Figure 5b, when the primary cooling temperature is 450 °C and the deformation temperature is 550 °C, the true stress-strain curve has an inflection point at the strain of 0.05 with the significant increase of the slope of the curve, indicating that phase transformation occurs to the material at this time. Moreover, as the deformation proceeds, the peak stress exceeds the strain rate of 0.1 s⁻¹. Thus, it can be considered that, during the tensile experiment, the low strain rate has given enough time to the supercooled austenite to transform into bainite [35], resulting in the increased deformation resistance. Conversely, at higher strain rates, the austenite does not have time to transform, thus, at this time, the material has a higher peak stress at a low strain rate.

After being completely austenitized, 38MnB5Nb will be transformed into different microstructures when cooled to different temperatures at different cooling rates. When cooled to temperature below M_s at a faster cooling rate, part of the austenite is transformed into martensite. Since the martensitic transformation is a non-diffusive transformation, the degree of transformation is affected by the cooling temperature. The transformation from austenite to ferritic pearlite or bainite occurs between the temperature of M_s and A_{c3} when cooling at a slower cooling rate. Figure 6a shows the effect of the primary cooling temperature on the peak stress when the deformation temperature is 550 °C. Under the strain rate of 1 s⁻¹, the difference of the peak stress between the primary cooling temperature of 200 °C and 450 °C has reaches 264.1 MPa, while the differences of the peak stress at the rate of 1 s⁻¹ at 650 °C and 750 °C are 101.0 MPa and 20.1 MPa, respectively. Due to the simultaneous deformation of the soft regions and the hard regions during the tailored properties hot forming by partition cooling, the large peak stress difference may lead to uncoordinated deformation, cracking, or significant spring-back after forming.

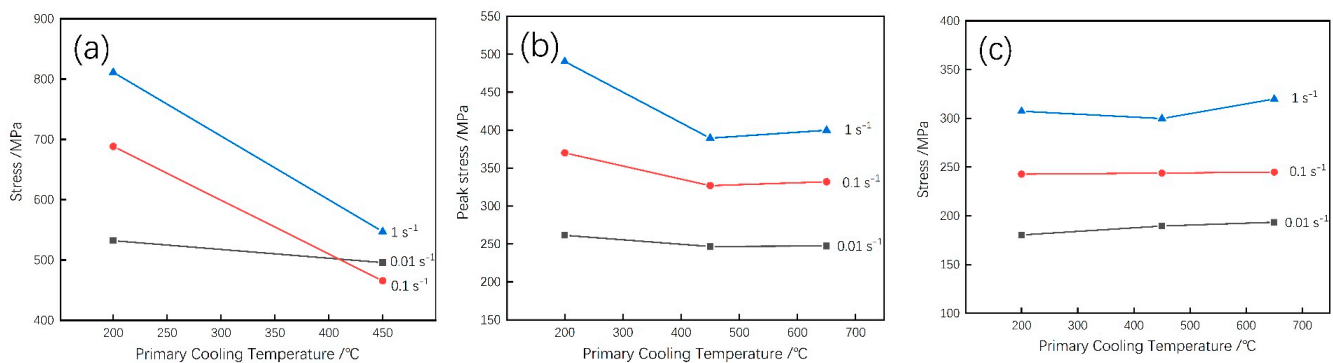


Figure 6. Influence of primary cooling temperature and strain rate at forming temperature of (a) 550 °C; (b) 650 °C; (c) 750 °C on peak stress.

It can be concluded that the primary cooling temperature has an impact on the high-temperature flow characteristics of 38MnB5Nb, so it is necessary to establish a unified

viscoplastic constitutive model that considering the primary cooling temperature to meet the requirements of TPP for numerical simulation.

5. Primary Cooling Temperature Coupled Constitutive Model

5.1. Establishment of a Constitutive Model

In order to summarize the evolution of recovery, dislocation density, grain size, and recrystallization volume fraction under deformation conditions such as high temperature creep, superplastic forming, and metal hot forming, Lin et al. [36,37] proposed a unified viscoplastic constitutive model, which has been proved to be reliable in predicting microstructural characteristic changes and macroscopic deformation behavior of various materials after numerous practices. In terms of tailored hot forming properties, Mu et al. [27] established a unified viscoplastic model coupled with the austenite volume fraction, which can better reflect hot deformation behavior of UHSS with different austenite volume fraction. Unlike Mu's work, the partition-cooling hot forming technology in this study requires primary cooling and tempering after complete austenitization. This means that the number of parameters to be fitted increases. Therefore, based on the viscoplastic constitutive model, the influence of the primary cooling temperature is considered in this study, and a unified viscoplastic constitutive equation coupled with the primary cooling temperature is established.

At high temperatures, considering the strain rate and strain hardening effect, the relationship between plastic strain rate and viscous stress can be expressed as:

$$\dot{\varepsilon}_p = \left\langle \frac{\bar{\sigma} - H - k}{K} \right\rangle^n \quad (1)$$

where $\dot{\varepsilon}_p$ is plastic strain rate, $\bar{\sigma}$ means flow stress, k indicates initial yield stress, H is internal stress due to isotropic hardening, K implies resistance coefficient, and n is the viscosity exponent. The McCauley brackets ensure that it only makes sense to enter the plastic stage after the material yields. Compared with Mu's work, this model can significantly reduce the amount of computation and facilitate parameter fitting [38].

Different primary cooling and tempering processes determine the microstructure of 38MnB5Nb during forming, which may include austenite, ferrite, pearlite, bainite and tempered martensite. Since pearlite is a mixture of alternating lamellae of ferrite and cementite in a single grain, the structure obtainable between A_{c3} and M_s can be regarded as a three-phase structure consisting of austenite, bainite and ferrite + pearlite, in order to simplify the calculation, ferrite + pearlite is classified as ferrite in this study [39,40]. On this basis, the overall plastic strain rate can be given as the combination of the related plastic strain rates of these four phases [41,42], the total strain rate can be expressed as:

$$\dot{\varepsilon}_p = \dot{\varepsilon}_{p.A}f_A + \dot{\varepsilon}_{p.B}f_B + \dot{\varepsilon}_{p.F}f_F + \dot{\varepsilon}_{p.M}f_M \quad (2)$$

where $\dot{\varepsilon}_{p.A}$, $\dot{\varepsilon}_{p.B}$, $\dot{\varepsilon}_{p.F}$, $\dot{\varepsilon}_{p.M}$ is the plastic strain rate of austenite, bainite, ferrite and tempered martensite, respectively, f_A , f_B , f_F , f_M indicates the volume fraction of austenite, bainite, ferrite and tempered martensite, respectively. It is assumed that after full austenitization the material is cooled at 30 °C/s and held or tempered for 30 s. It is assumed that martensite is completely transformed into tempered martensite after tempering. According to the DANTE heat treatment simulation software (DANTE Solutions, Inc., Cleveland, OH, USA), the relationship between the volume fraction and the primary cooling temperature is estimated as:

$$\begin{cases} f_M = 1 - \exp[-m_1(m_2 - T)] \\ f_B = b_1 \exp\left[-\left(\frac{T-b_2}{b_3}\right)^2\right] \\ f_F = c_1 \exp\left[-\left(\frac{T-c_2}{c_3}\right)^2\right] \\ f_A = 1 - f_B - f_F - f_M \end{cases} \quad (3)$$

The volume fraction of each phase at each primary cooling temperature was calculated by the software, and obtained by nonlinear fitting, where $m_1 = 0.032$, $m_2 = 571$, $b_1 = 0.79$, $b_2 = 711.8$, $b_3 = 95.4$, $c_1 = 0.82$, $c_2 = 929.4$, $c_3 = 59.3$, which are the material constants (as shown in Figure 7).

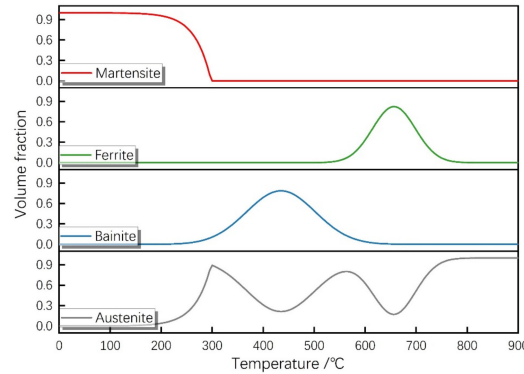


Figure 7. Relationship between volume fraction of each phase and primary cooling.

When 38MnB5Nb is formed at high temperature, the evolution of the microstructure is based on the evolution of dislocation density; hence, dislocation density is selected as an internal variable to describe the isotropic hardening behavior of the material. The dislocation density evolution equation is:

$$\dot{\bar{\rho}} = A(1 - \bar{\rho})|\dot{\epsilon}_p| - C\bar{\rho}^\lambda \tag{4}$$

The first term considers dislocation growth and dynamic recovery processes, and the second term considers dislocation static recovery processes. $\bar{\rho}$ is the regularized dislocation density, and the evolution of the dislocation density is limited between 0 and 1 by regularization. $\dot{\bar{\rho}}$ is the growth rate of dislocation density, and A , C and λ are the material constants. The hardening stress and dislocation density of material deformation can be expressed as:

$$H = B\bar{\rho}^{0.5} \tag{5}$$

That is, the evolution equation of the isotropic hardening variable H is expressed as:

$$\dot{H} = 0.5B\bar{\rho}^{-0.5}\dot{\bar{\rho}} \tag{6}$$

where B is the material constant, which shows that the isotropic hardening is mainly caused by the accumulation and interaction of dislocation. However, the dislocation density decreases due to the dynamic and static recovery, which makes the material soften.

The total strain ϵ can be divided into elastic strain and plastic strain. The elastic strain satisfies Hooke’s law, and considering the viscosity equation, phase transformation equation, work hardening equation, dislocation density evolution equation and Hooke’s law, a viscoplastic constitutive equations system describing 38MnB5Nb at different primary cooling temperatures can be obtained:

$$\begin{cases} \dot{\epsilon}_{p,X} = \left\langle \frac{\bar{\sigma} - H_X - k_X}{K_X} \right\rangle^n & X = A, B, F, M \\ \dot{\epsilon}_p = \dot{\epsilon}_{p,A}f_A + \dot{\epsilon}_{p,B}f_B + \dot{\epsilon}_{p,F}f_F + \dot{\epsilon}_{p,M}f_M \\ \dot{\bar{\rho}}_X = A_X(1 - \bar{\rho}_X)|\dot{\epsilon}_{p,X}| - C_X\bar{\rho}_X^{\lambda_X} & X = A, B, F, M \\ \dot{H}_X = 0.5B\bar{\rho}_X^{-0.5}\dot{\bar{\rho}}_X & X = A, B, F, M \\ \dot{\sigma} = E_0(\dot{\epsilon}_T - \dot{\epsilon}_p) \end{cases} \tag{7}$$

In the viscoplastic constitutive equations system, the material constants k , K , A , B , C , and E_0 are assumed to be related to temperature, and the relationship between temperature and the material constants in the Arrhenius equation is introduced as:

$$\begin{cases} k = k_i \exp(Q_k/RT) \\ K = K_i \exp(Q_K/RT) \\ A_X = A_{iX} \exp(Q_{AX}/RT) & X = A, B, F, M \\ B = B_i \exp(Q_B/RT) \\ C_X = C_{iX} \exp(-Q_{CX}/RT) & X = A, B, F, M \\ E_0 = E_i \exp(Q_E/RT) \end{cases} \quad (8)$$

where k_A , k_B , k_F , k_M are the initial yield stress of austenite, bainite, ferrite, and tempered martensite, respectively. Assume that $k_B = m_b \cdot k_A$, $k_F = m_f \cdot k_A$, $k_M = m_m \cdot k_A$, $K_B = n_b \cdot K_A$, $K_F = n_f \cdot K_A$, $K_M = n_m \cdot K_A$, which are the material constants. The equations have a total of 35 material constants that must be determined: k_i , K_i , A_{iX} , B_i , C_{iX} , E_i , Q_k , Q_K , Q_{AX} , Q_B , Q_{CX} , Q_E , m_b , m_f , m_m , n_b , n_f , n_m , λ_X , n ($X = A, B, F, M$). R is the universal gas constant, and T is the absolute temperature in K.

5.2. Calibration and Verification of the Constitutive Model

The unified viscoplastic constitutive equations of 38MnB5Nb established in this study are nonlinear and highly coupled with each other. In this study, MATLAB software (version 2021b, MathWorks, Inc., Natick, MA, USA) and a genetic algorithm are used to determine the material constants in the constitutive equations. The solution of the ordinary differential equations system adopts the forward Euler method, and the approximate solution of the differential equations is obtained with a fixed step size. Then the objective function is used to evaluate the difference between the approximate solution of the differential equations system and the true stress-strain curve obtained by experiments, so as to judge the group of the material constants. The relevant settings in the genetic algorithm are as follows: the population size is 200, the number of genetic algebras is set to be 3000 generations, the population crossover probability is 0.9 while the population mutation probability is 0.05, the optimization accuracy is 10^{-6} . The objective function adopts the functional form proposed by Cao and Lin [35,36], which is expressed as follows:

$$f(X) = \frac{1}{M} \sum_{j=1}^M \left\{ \frac{1}{N_j} \sum_{i=1}^{N_j} \left(\ln \frac{\sigma_{ij}^c}{\sigma_{ij}^e} \right)^2 \right\} \quad (9)$$

where X is the material constant vector to be determined. M is the number of stress-strain curves obtained by the test. N_j is the number of tested data points taken on the j^{th} stress-strain curve, and σ_{ij}^c is the calculation of the flow stress at strain i . σ_{ij}^e is the experimental value of the flow stress at strain i .

The fitting effect of the constitutive model is quantitatively evaluated. Relative coefficient (R), average absolute relative error (AARE) and root mean square error (RMSE) are selected as indicators to evaluate the fitting effect of the two models from the prospect of statistics. The expressions of the three statistics are as follows.

$$R = \frac{\sum_{k=1}^N (E_k - \bar{E})(P_k - \bar{P})}{\sqrt{\sum_{k=1}^N (E_k - \bar{E})^2 \sum_{k=1}^N (P_k - \bar{P})^2}} \quad (10)$$

$$\text{AARE}(\%) = \frac{1}{N} \sum_{k=1}^N \left| \frac{E_k - P_k}{E_k} \right| \times 100 \quad (11)$$

$$\text{RMSE} = \sqrt{\frac{1}{N} \sum_{k=1}^N (E_k - P_k)^2} \quad (12)$$

where E_k implies the experimental data points, P_k is the temperature value calculated by the fit model, \bar{E} and \bar{P} represent the mean values of the experimental data and fitted values, respectively. N is the total number of data points. Figure 8 indicates the linear correlation analyzed from all data. The predicted stress is in good agreement with the experimental stress. $R > 0.95$ was considered a significant correlation [43].

The comparison of the stress-strain values calculated by the experiment and by the unified viscoplastic constitutive model at different primary cooling temperatures, deformation temperature and strain rates are shown in Figure 9, in which the green, blue and red colors represent the strain rate of 0.01 s^{-1} , 0.1 s^{-1} , 1 s^{-1} . The symbol is the true stress-strain of the experimental data, and the solid line is the calculated value according to the constitutive model. It can be seen that the predicted values of the constitutive model are in good agreement with the experimental values. Since the constitutive model established in this paper does not take into account the effect of phase transformation during recrystallization and deformation, this may lead to some errors in predictions under low strain. The material constants for the proposed constitutive model are shown in Table 2.

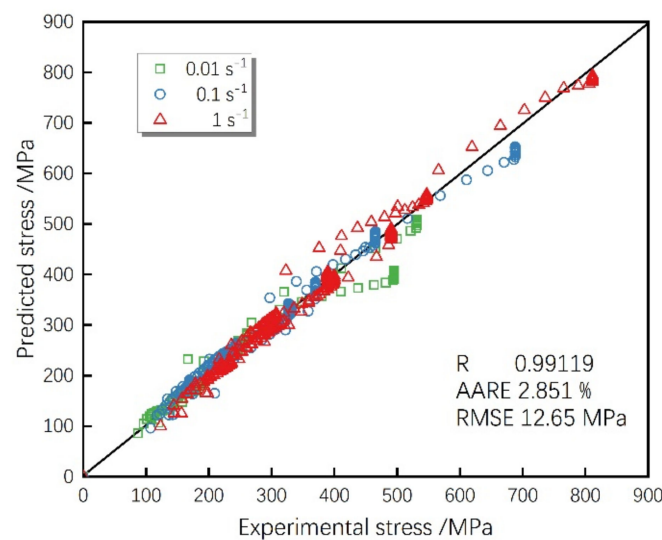


Figure 8. Linear correlation plot of Predicted stress-Experimental stress.

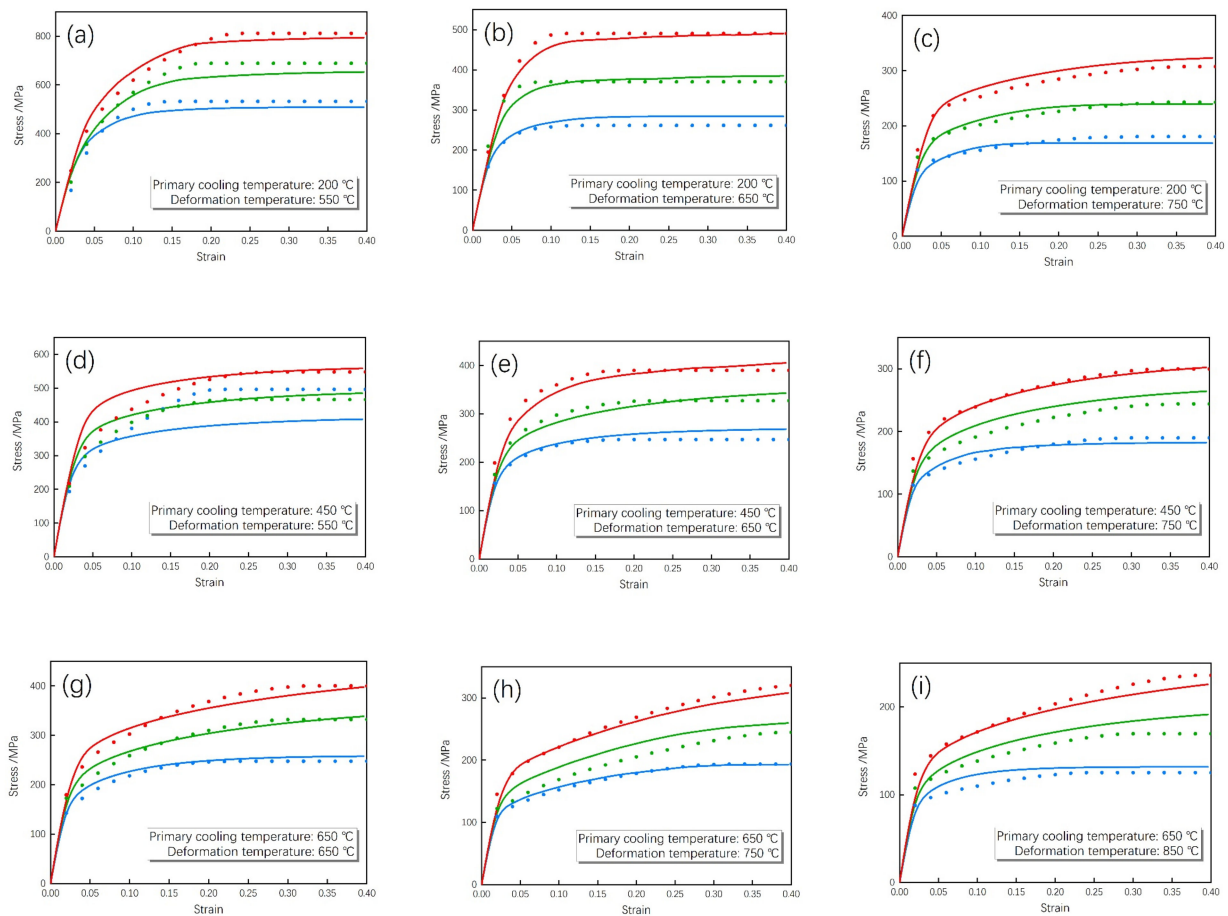


Figure 9. Comparison of experimental and calculated strain-stress curves at different primary cooling temperatures, deformation temperatures and strain rates. Blue, green and red colors represent the strain rate of 0.01 s^{-1} , 0.1 s^{-1} , 1 s^{-1} . Primary cooling at $200 \text{ }^{\circ}\text{C}$, deformation at (a) $550 \text{ }^{\circ}\text{C}$, (b) $650 \text{ }^{\circ}\text{C}$, (c) $750 \text{ }^{\circ}\text{C}$, primary cooling at $450 \text{ }^{\circ}\text{C}$, deformation at (d) $550 \text{ }^{\circ}\text{C}$, (e) $650 \text{ }^{\circ}\text{C}$, (f) $750 \text{ }^{\circ}\text{C}$, primary cooling at $650 \text{ }^{\circ}\text{C}$, deformation at (g) $650 \text{ }^{\circ}\text{C}$, (h) $750 \text{ }^{\circ}\text{C}$, (i) $850 \text{ }^{\circ}\text{C}$.

Table 2. The material constants for the proposed constitutive model.

k_i	Q_k	K_i	Q_K	A_{iA}	Q_{AA}	A_{iB}
4.834	985.4	2.524	3.551×10^4	3.525	6.811×10^3	4.335
Q_{AB}	A_{iF}	Q_{AF}	A_{iM}	Q_{AM}	B_i	Q_B
7.760×10^3	32.147	9.436×10^3	10.117	1.411×10^4	78.021	6.779×10^3
C_{iA}	Q_{CA}	C_{iB}	Q_{CB}	C_{iF}	Q_{CF}	C_{iM}
5.289	2.878×10^4	111.458	3.763×10^4	9.725	3.629×10^4	149.906
Q_{CM}	λ_A	λ_B	λ_F	λ_M	m_b	m_f
6.867×10^3	1.288	0.479	35.791	4.375	4.206	4.081
m_m	n_b	n_f	n_m	E_i	Q_E	n
18.105	1.069	0.712	1.925	556.589	2.149×10^4	10.017

6. Interfacial Heat Transfer Coefficient

In the TPP, the real-time data of the heat transfer coefficient of the partition cooling process with temperature under different cooling conditions are necessary to make the simulation closer to the actual production and improve the accuracy of the simulation. During the partition cooling process of 38MnB5Nb, a large amount of heat exchange occurs between the hot UHSS blank and the cooling medium. The cooling rate and the phase

transition process of the blank will be affected by the different degrees of heat exchange, which will eventually affect the mechanical properties of the part.

The degree of the heat exchange between the surface of the blank and the medium can be expressed by the interfacial heat transfer coefficient. In the TPP, as one of the essential boundary conditions, the interfacial heat transfer coefficient is a parameter that must be input in the simulation analysis, which directly affects the accurate simulation of multi-field coupling, temperature field, organization field, and stress field. Therefore, the study of the interfacial heat transfer coefficient under different cooling conditions can help set the heat transfer coefficient in the numerical simulation process of partition cooling and tailored hot forming of 38MnB5Nb.

6.1. Experiment with Single-Nozzle Cooling

The experiment equipment is shown in Figure 10. The gas jet is generated by the self-made air compressor, passing through the filter, the pressure tank, and the valve to form a fully developed free jet, and at last, the gas jet is ejected from the circular straight pipe. The uniform temperature in the cooling region, narrow temperature transition region and controllable shape of the cooling region need to be satisfied during the partition cooling process. Meanwhile, the return air system (Figure 10) is designed to reduce the influence of lateral side flow and dry ice particle sputtered in the high-temperature region during the cooling process. The bottom side of the return air system is a 20 mm × 20 mm square, which is in contact with the surface of the blank, while the top side is a negative pressure region to guide and discharge part of the heat exchange air. The dry ice particles are brought into the gas jet pipeline from the block dry ice and the valve to form a dry ice-air mixed gas. The inner diameter of the circular straight pipe is $D = 4$ mm, the length is $L = 40$ mm, and the height of the nozzle from the surface of the workpiece is 20 mm. The lower part of the test workpiece is insulated with aluminum silicate fiber, while the temperature of the workpiece is measured by a K-type thermocouple and recorded by the data acquisition system. The location of the temperature measurement point is shown in Figure 11. Thermocouples are arranged at intervals of 10 mm from the central position, with a total of 8 temperature measurement points (two in the central position). The size of the 38MnB5Nb blank used in the experiment is 250 mm × 150 mm × 2.0 mm. This temperature measurement data includes the blank's transfer process (about 10 s).

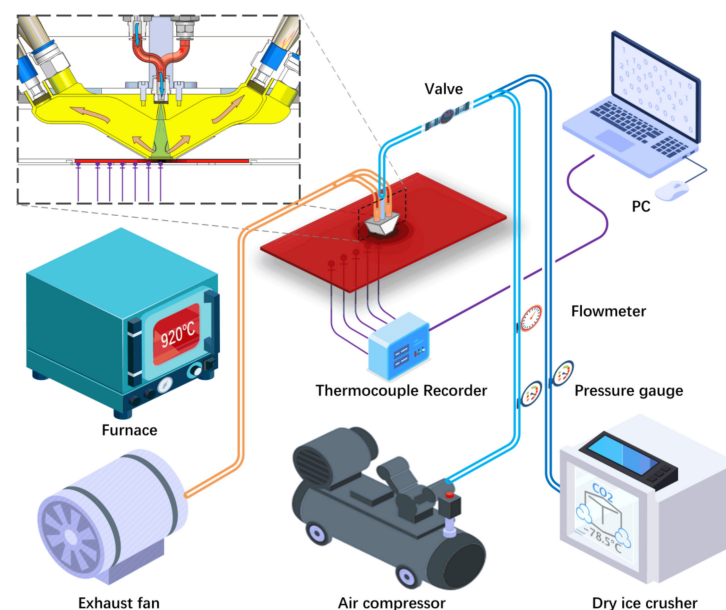


Figure 10. Diagram of the single-nozzle cooling experiment equipment.

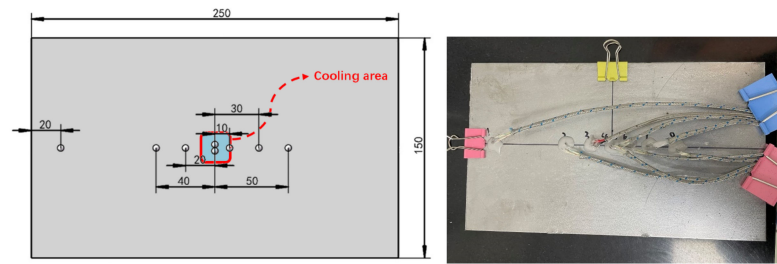


Figure 11. Schematic diagram of the welding position of the thermocouple (unit in mm).

6.2. Solving for Inverse Heat Conduction Problem (IHCP)

The corresponding position of each thermocouple under the temperature measurement model is regarded as a 1D thermal conductivity model, and its geometry model is shown in Figure 12.

The governing equation of the 1D thermal conductivity model is:

$$\alpha \frac{\partial^2 T}{\partial x^2} = \frac{\partial T}{\partial t} \quad 0 < x < L, \quad t > 0 \text{ where the thermal diffusivity } \alpha = \frac{k}{\rho C_p} \quad (13)$$

The upper wall ($x = 0$) of the 38MnB5Nb blank is the first boundary condition, and the lower wall ($x = L$) is the third boundary condition, namely:

$$k \frac{\partial T(x, t)}{\partial x} = q(x, t) \quad x = 0, \quad t > 0 \quad (14)$$

$$\frac{\partial T(x, t)}{\partial x} = 0 \quad x = L, \quad t > 0 \quad (15)$$

the initial condition is:

$$T(x, t) = T_0 \quad 0 < x < L, \quad t = 0 \quad (16)$$

k is the thermal conductivity of the material, ρ means the material density, and C_p indicates the specific heat capacity at constant pressure of the material. Considering that 38MnB5Nb will undergo different degrees of phase transition under different cooling states, k and C_p are considered to be related to the temperature and cooling rate, as shown in Figure 13a,b. Material parameters are calculated by JMatPro® software version 7.0.

When convective heat transfer occurs, the heat flow is calculated according to Newton’s cooling formula:

$$q = h(T_w - T_{gas}) \quad (17)$$

where T_w is the temperature of the upper surface of the blank, h is the interface heat transfer coefficient, of which the unit is $W/(m^2 \cdot K)$, and T_{gas} is the fluid temperature ($^{\circ}C$), which is obtained by measurement, or considered as a constant. The heat fluxes q , and T_w can solve IHCP, as shown in Figure 14. The calculation is introduced below.

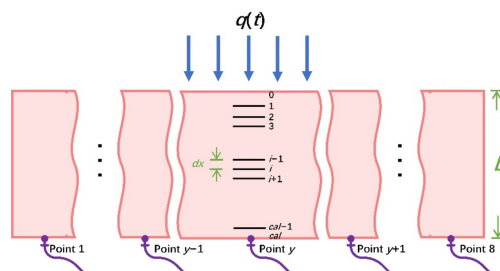


Figure 12. Geometry model of heat transfer.

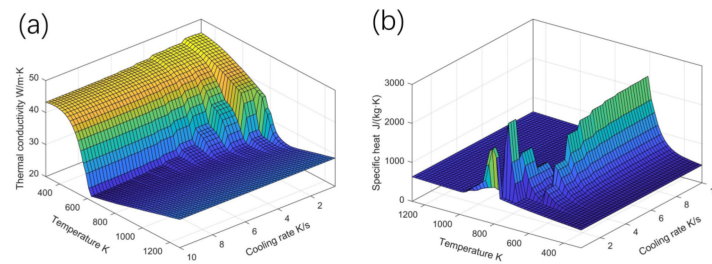


Figure 13. (a) Thermal conductivity and cooling rate and temperature; (b) specific heat of material and cooling rate and temperature.

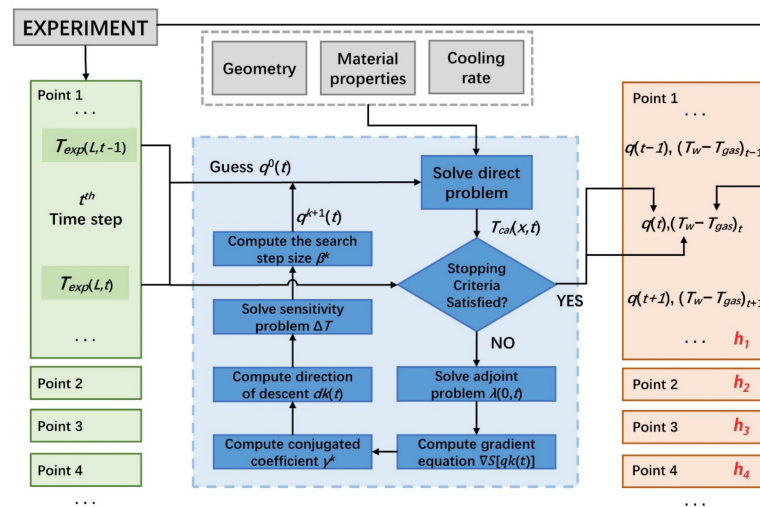


Figure 14. Solving IHCP Flowchart.

The heat conduction problem is to solve the temperature fluctuation of the bottom surface according to the temperature fluctuation of the upper surface cooled by the medium, which is a fixed solution problem. However, the inverse problem of heat conduction is to solve the temperature fluctuation of the top surface cooled by the medium according to the temperature fluctuation of the bottom surface, which is an optimization problem. The optimized objective function is shown as:

$$S[q(t)] = \int_{t=0}^{t_f} \{T_{exp}(L, t) - T_{cal}(L, t)\}^2 dt \tag{18}$$

where T_{exp} is the measured temperature obtained by the thermocouple of the bottom surface, T_{cal} is the calculated temperature obtained by solving the inverse problem of the bottom surface and t_f is the final time.

H is estimated via the conjugate gradient method (CGM) and the adjoint problem function.

Step 1: Take an initial guess $q^0(t)$ for the heat flux function $q(t)$. The number of iterations k is set as $k = 0$.

Step 2: Solve the 1D heat transfer problem and calculate $T(x, t)$ from $q^k(t)$.

Step 3: Check the stopping criterion until the function value $S[q(t)]$ reaches the tolerance ϵ . Output the heat flux function $q(t)$ if the tolerance satisfied the stopping criterion, and continue if not.

Step 4: Knowing $T_{cal}(L, t)$ and the measured temperature $T_{exp}(L, t)$, solve the accompanying problem by the method in the literature [44] and calculate the gradient $\nabla S[qk(t)]$.

Step 5: Knowing $\nabla S[q^k(t)]$, γ^k and the descending direction $d^k(t)$ are calculated according to the following equation. γ^k is the conjugate coefficient obtained from the following Fletcher-Reeves expression.

$$\gamma^k = \frac{\int_{t=0}^{t_f} \{ \nabla S [q^k(t)] \}^2 dt}{\int_{t=0}^{t_f} \{ \nabla S [q^{k-1}(t)] \}^2 dt} \tag{19}$$

For the first iteration, $\gamma^0 = 0$.

$$d^k(t) = \nabla S [q^k(t)] + \gamma^k d^{k-1}(t) \tag{20}$$

Step 6: Set $\Delta q^k(t) = d^k(t)$ and obtain $\Delta T(L, t)$ by solving the sensitivity problem [45].

Step 7: Knowing $\Delta T(L, t)$, the search step length β^k is calculated from the following equation

$$\beta^k = \frac{\int_{t=0}^{t_f} [T(L, t) - Y(L, t)] \Delta T(L, t) dt}{\int_{t=0}^{t_f} [\Delta T(L, t)]^2 dt} \tag{21}$$

Step 8: Knowing the β^k and $d^k(t)$, a new estimated $q^{k+1}(t)$ is calculated according to the following equation and then return to Step2.

$$q^{k+1}(t) = q^k(t) - \beta^k d^k(t) \tag{22}$$

The temperature change of the bottom surface of the 38MnB5Nb blank under 0.1 MPa jet pressure and 0.5 MPa jet pressure mixed with dry ice particles with a flow rate of 10 g/s and a diameter of about 100 μm is measured by experiments (Figure 15).

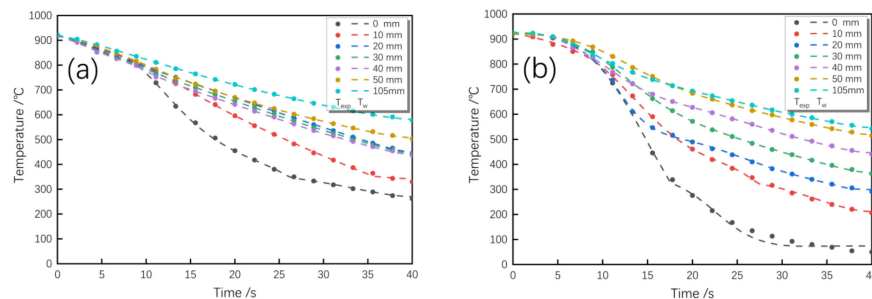


Figure 15. Temperature measurement curves. (a) 0.1 MPa compressed air; (b) 0.5 MPa compressed air mixed with dry ice particles.

For the hot-state experiment of the cooling blank under the partition jet condition of the 38MnB5Nb blank, the temperature-time curve can be used to intuitively understand the temperature change of each region of the selected blank during the cooling process. As the jet has an influence on the temperature difference, the cooling rate at the center of the blank is faster. Under the mixed jet of 0.5 MPa dry ice and air, the cooling capacity of the mixed jet is improved due to the contact between the dry ice and the hot blank as the dry ice particles sublime and absorb heat, during which the maximum cooling rate can reach 68 $^{\circ}\text{C}/\text{s}$. Affected by the return air system with negative pressure, the effect of the jet flow is reduced when it deviates from the core jet region. The cooling rate is lower in the region ≥ 30 mm.

Figure 16 shows the relationship between the temperature and the heat transfer coefficient at each region. It finds that when the temperature is in the range of 850–920 $^{\circ}\text{C}$, the change of heat transfer coefficient and temperature is not obvious, as the process in this temperature range is the process of blank transfer and air cooling. Affected by the 0.5 MPa dry ice mixed with air jet in the central region, the heat transfer coefficient impacted by

the jet significantly rises as the temperature decreases, reaching a maximum value of $1900 \text{ W}/(\text{m}^2\cdot\text{K})$ at about $300 \text{ }^\circ\text{C}$, which is comparable to the heat transfer coefficient of air-mist cooling. The heat transfer coefficient in the non-jet impingement region is predominantly affected by radiation and lateral flow. Under the influence of 0.1 MPa compressed air, the heat transfer coefficient in the central region increases at first and then decreases, with a maximum value of about $570 \text{ W}/(\text{m}^2\cdot\text{K})$.

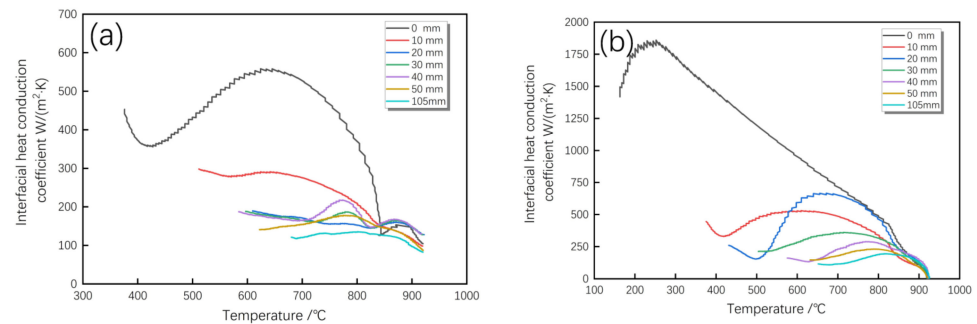


Figure 16. Interfacial heat conduction coefficient. (a) 0.1 MPa compressed air; (b) 0.5 MPa compressed air mixed with dry ice particles.

Considering the temperature changes of the blank under different cooling conditions, the narrow transition regions' width should be satisfied while ensuring the process requirements. The primary cooling step of TPP-S is realized by 0.1 MPa compressed air jet, while that of TPP-F is realized by 0.5 MPa compressed air and dry ice mixture since it needs to be cooled to about M_f and requires a higher heat transfer coefficient.

Figure 17 shows the linear correlation analyzed from all data. It can be seen that the temperature calculated by the interface heat transfer coefficient h obtained by the inverse heat transfer method is accurate with the experimental results.

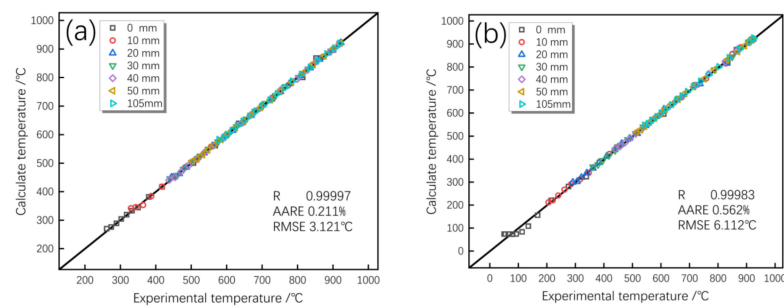


Figure 17. Linear correlation plot of fitted values-experimental values. (a) 0.1 MPa compressed air; (b) 0.5 MPa compressed air mixed with dry ice particles.

7. FEM of TPP

7.1. Applications

The designed tailored properties hot forming system (Figure 18) for 38MnB5Nb blank is predominantly composed of austenitizing furnace FO810 (Yamato Scientific Co., Ltd., Tokyo, Japan), tempering furnace FO810 (Yamato Scientific Co., Ltd., Tokyo, Japan), and self-made equipment, partition cooling device ("Cold Printer"), U-shaped part forming die, 100 T press, air compressor and temperature monitoring system. The austenitizing furnace is first heated and kept at $920 \text{ }^\circ\text{C}$, while the tempering furnace needs to be heated and kept at $900 \text{ }^\circ\text{C}$, according to the TPP-S and TPP-F requirements respectively. The cold printer is mainly composed of a cooling system, exhaust fan and temperature monitoring system. The cooling system consists of 12 sets of cooling units with a cooling region of $20 \text{ mm} \times 20 \text{ mm}$ arranged in a line. Each unit can be independently controlled by the electronic control system, and the upper and bottom sides can be cooled at the same time.

The “Cold Printer” realizes automatic feeding through the control system. When the region to be cooled reaches the cooling unit, the cooling program starts to run, and the flow rate of the nozzle and the flow of dry ice particles are controlled according to the required primary cooling temperature difference to achieve partition cooling of the high-temperature blank. The reference part is a U-shaped piece, which is achieved through the hot forming die system shown in Figure 19 mounted on the 100 T press. The die system is mainly made up of a lower die, a punch, a binder, and 8 nitrogen springs. The blank processed by partition cooling, and tempering is placed on the lower die and fixed in the center by positioning pins before the punch and the binder moving downward from the initial position (246 mm above the upper surface of the lower die) at a speed of 50 mm/s. After the binder contact the blank, a force of 20 kN is applied, while the punch continues to move downward for 54 mm at a speed of 20 mm/s. After reaching the position, a holding pressure of 200 kN is applied for 15 s.

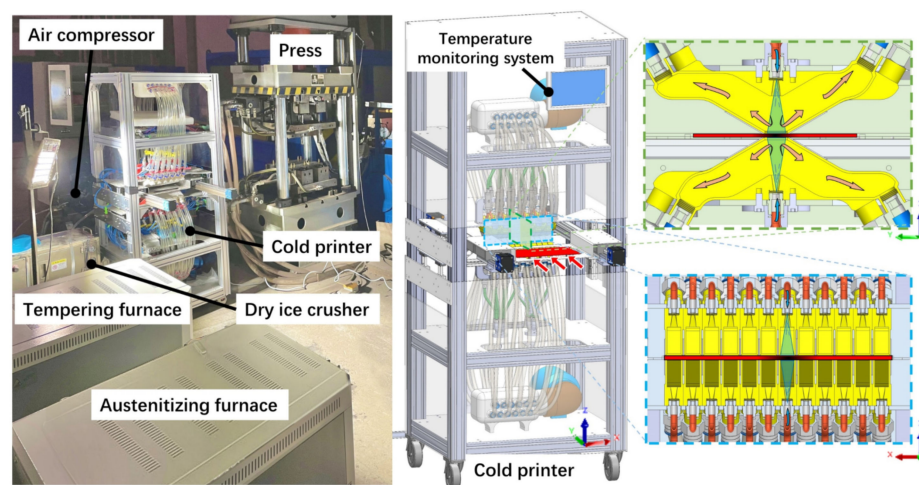


Figure 18. TPP system.

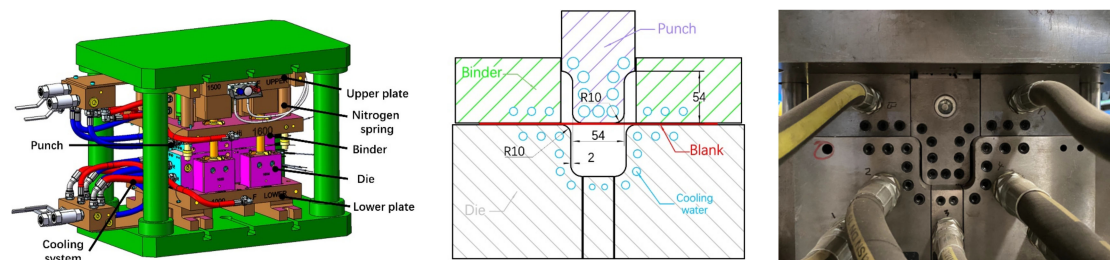


Figure 19. Die system for hot forming U-shaped parts.

The detailed partition cooling and tailored properties hot forming are as follows. The 250 mm (L) × 150 mm (W) blank is put into a 920 °C austenitizing furnace for 7 min before being taken out and put into the “Cold printer” for cooling, of which the transfer time is about 10 s. The blank is cooled for 10 s by the 0.1 MPa compressed air jet in the TPP-S or by the 0.5 MPa dry ice mixed jet in TPP-F before being tempered for 30 s in the 900 °C tempering furnace. Then the blank is transferred to the press for forming of which the transfer time is about 10 s, while the die is filled with cooling water and maintained for 15 s.

7.2. Numerical Modelling

The hot forming of UHSS is an extremely complex nonlinear thermo-mechanical coupling process. In order to improve the calculation efficiency, the original model was simplified to a 1/4 symmetrical geometric model, as shown in Figure 20. In this model, the die is divided into 28,080 units according to C3D8T, and the blank is divided into 1180 units

according to S4RT. The thickness of the blank is 2 mm, and the number of integral points along the thickness direction is 3. Meanwhile, the binder, the die, and the punch are set as rigid bodies. The interfacial heat transfer coefficient between the die system and the blank changes during the forming process. For example, when the blank is in complete contact with the die, the interfacial heat transfer coefficient is related to the pressure, but when there is no contact, the interfacial heat transfer coefficient is related to the gap size. The set of interfacial heat transfer coefficient is based on the literature [46,47], while the friction coefficient between the blank and the die system is set to 0.35 [21,48]. Constitutive material models can be implemented into ABAQUS 2020/Explicit software using the explicit user materials subroutine (VUMAT), which can use and update solution-dependent state variables, e.g., plastics strain (ϵ_p), dislocation (ρ). The developed unified viscoplastic constitutive equation system coupled with the primary cooling temperature model were programmed into VUMAT using the FORTRAN language. The relevant physical property parameters of the blank are obtained according to a published paper [46–49]. The interfacial heat transfer coefficient between the blank and environment during austenitizing and tempering is a function of temperature, of which the setting method in [50] is adopted. The interfacial heat transfer coefficient calculated above is adopted in the primary cooling process. Considering the field specificity of the square nozzle, the interfacial heat transfer coefficient between the data points is calculated by the method of linear interpolation. In order to reduce the calculation time and improve the calculation efficiency, a reasonable mass amplification factor is set in the simulation process.

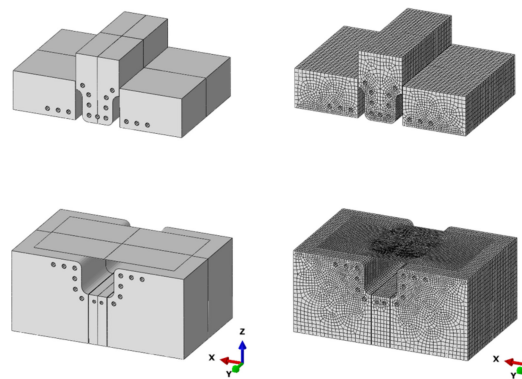


Figure 20. Finite element model for partition-cooling hot forming simulation.

7.3. Results and Discussion

Unlike traditional hot forming technology, the partition-cooling hot forming technology requires specific cooling of the blank before forming to achieve a specific microstructure distribution in order to satisfy the tailored strength requirements. Figure 21 displays the temperature distribution of the blank after partition cooling. The minimum temperature of the central blank under TPP-S and TPP-F is about 453.7 °C and 201.5 °C, respectively. Martensite is formed during the process. The uncooled region is kept above 650 °C with the width of the transition regions being about 20 mm. The simulation results (Figure 22) illustrate that the temperature of the central blank under the two processes is about 456 °C and 196 °C, respectively, which are in good agreement with the experimental results. The temperature field distribution of the two processes after being placed in the tempering furnace at 900 °C for 30 min is shown in Figure 23. The time-temperature transformation (TTT) “nose tip” region of 38MnB5Nb is about 600–650 °C [51]. The tempering temperature should not be too high, otherwise, the amount of transformed ferrite and pearlite is too small to meet the requirements of the tailored properties. Though the primary cooling temperature of TPP-F is only about 200 °C, the temperature in this region reaches 588 °C after tempering due to the small cooling region and the high tempering temperature. The temperature field is used as the initial condition for both forming simulations.

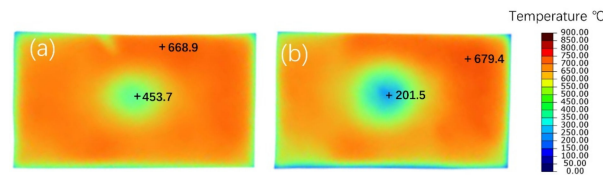


Figure 21. The temperature distribution of the blank after cooling in the acquisition region of the thermal imager. (a) TPP-S; (b) TPP-F.

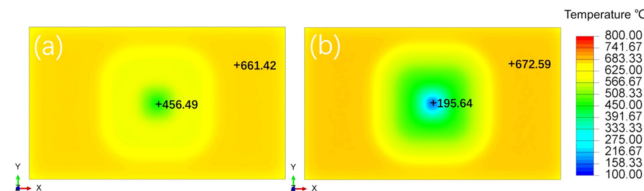


Figure 22. The simulated temperature distribution of the blank after primary cooling. (a) TPP-S; (b) TPP-F.

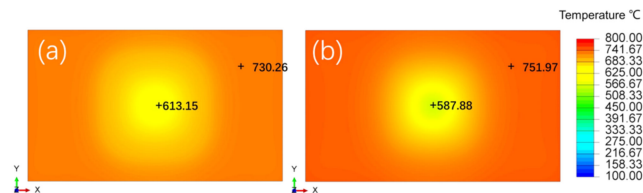


Figure 23. The simulated temperature distribution of the blank after tempering. (a) TPP-S; (b) TPP-F.

The temperature field in the forming stage when the blank transferring to the press is shown in Figures 24 and 25. When the stroke is 27 mm, the contact time between the blank and the die is 1.5 s. Because of the heat conduction during contact between the blank and the die, the temperature of the flange edge in contact with the binder drops the fastest, to 123 °C and 136 °C, corresponding to the two tailored properties hot forming technology. Meanwhile, the bottom and side surfaces of the U-shaped part below the punch and the die have higher temperatures, which decrease during the formation stage. The pressure holding stage in the hot forming is very essential, as it may lead to the uncomplete cooling of the blank or the microstructure transformation if the pressure holding time is insufficient, which will eventually cause uneven stress distribution, resulting in the deformation and spring-back of the blank. It can be seen that, after pressure holding for 15 s, the temperature of the whole blank drops below 120 °C, and the stress distribution is more uniform than when the stroke reaches 54 mm.

In the initial stage of forming, the equivalent stress of the contact position between the blank and the punch is the largest, and flat areas farther from the punch fillet are less stressed. As the stroke increases, the maximum equivalent stress is transferred to the sidewall region, because in the process of hot forming, the part of the blank that first contacts the punch is deformed, and is subjected to tension and bending stress. Due to the action of pressure, the heat of the sheet will be transferred to the cold die, resulting in the temperature decreasing, and the deformation resistance increasing. When the punch continues to move, more force is required to deform the blank. It can be seen that the largest strain occurs at the fillet and sidewall, which at the region shows a higher strain tendency. The equivalent plastic strain reaches 0.28, and the thickness thins to 1.91 mm.

The gradient microstructure formed by cooling also has a significant impact on the stress field distribution. The stress in the bottom center is larger, at which the maximum stress reaches 345 MPa after pressure holding for TPP-S and 743 MPa for TPP-F due to the high deformation resistance of the tempered martensite structure at the center of the bottom. In the spring-back stage without constraining, the residual stress can be released by plastic deformation, and the maximum residual stress in the two processes after spring-back drops to 305 MPa and 545 MPa, respectively.

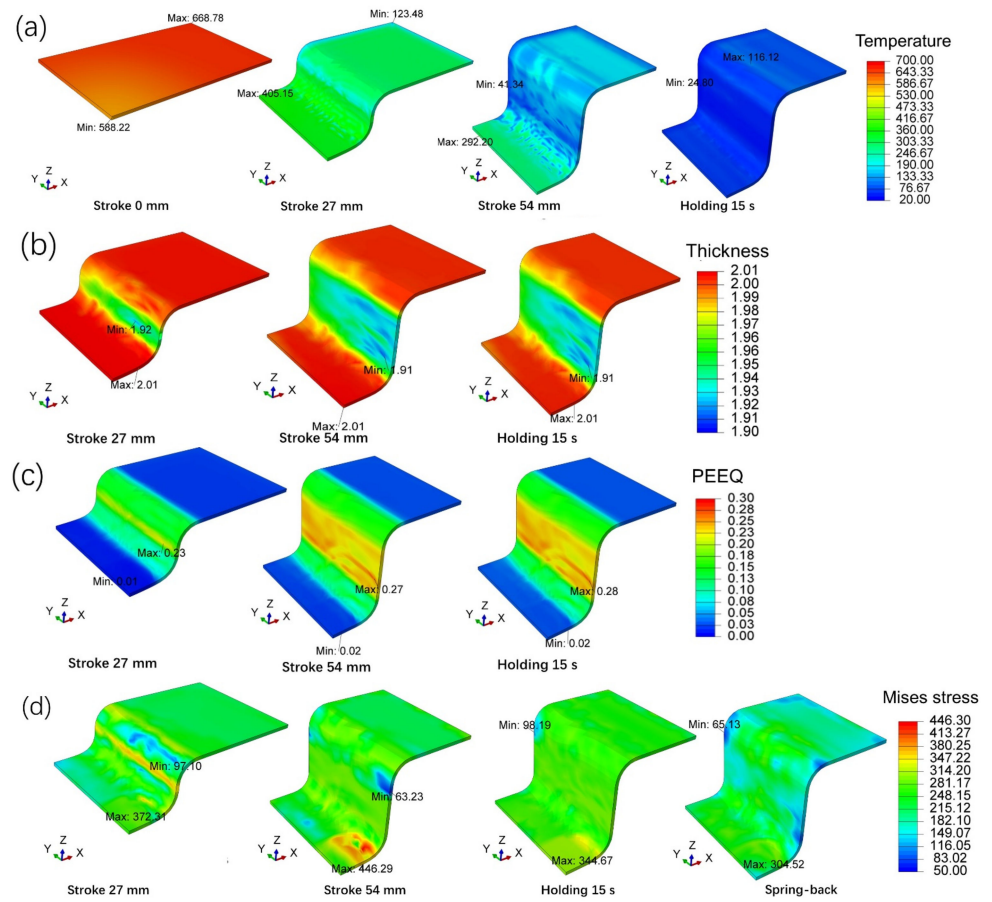


Figure 24. (a) Temperature; (b) Thickness; (c) Strain; (d) Stress with TPP-S.

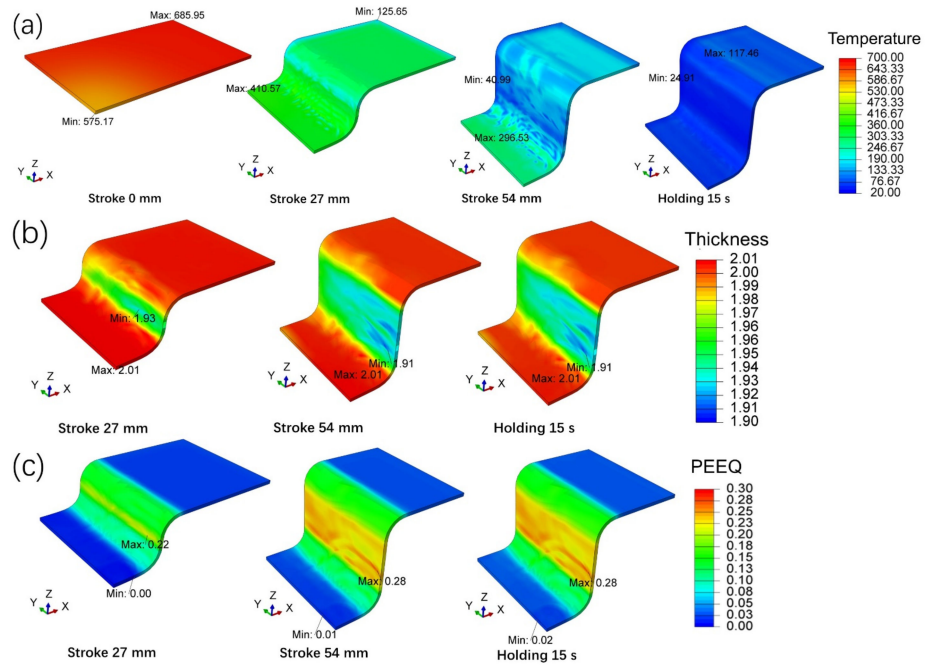


Figure 25. Cont.

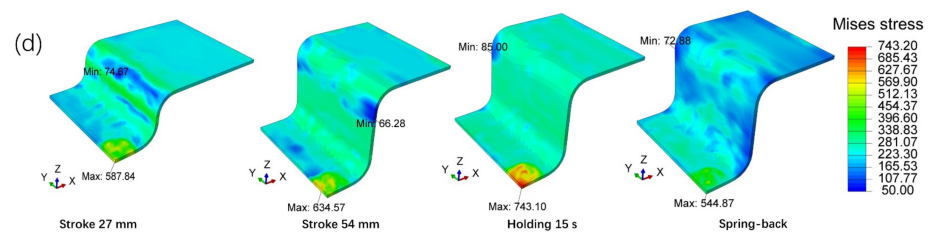


Figure 25. (a) Temperature; (b) Thickness; (c) Strain; (d) Stress with TPP-F.

The minimum thickness measured on the wall is about 1.91–1.92 mm, with a thinning rate of about 4.5%. There is no risk of rupture in this region. The flange edge contact with the binder and the bottom contact with the punch are slightly thickened to 2–2.02 mm due to radial and circumferential stress. Figure 26 points out that the numerical simulation is in good agreement with the experimental results.

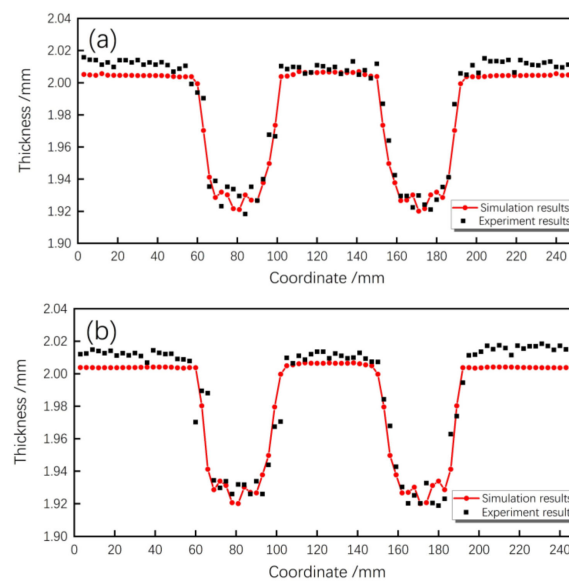


Figure 26. Comparison of the thickness between numerical simulation of the U-shaped part and the blank used in the experiment. (a) TPP-S; (b) TPP-F.

A material with a higher yield strength will have a greater ratio of elastic to plastic strain and will exhibit more spring-back than material with a lower yield strength, due to the high yield strength of 38MnBNb5, which leads to the spring-back of the parts after forming, especially under TPP as the UHSS after forming has different microstructure, strain, stress and temperature distribution from traditional hot forming parts. In this experiment, based on the analysis of the stress-strain field, the temperature transition regions of the regional cooling process are found to be only about 20 mm, and the uneven distribution of the stress-strain field does not touch the fillet and sidewall regions, with the bottom in a plane stress state. The spring-back is small under the two processes, with a maximum spring-back angle of no more than 1° . The numerical simulation of the constitutive model established in this study has a high degree of agreement with the experimental results (Figure 27).

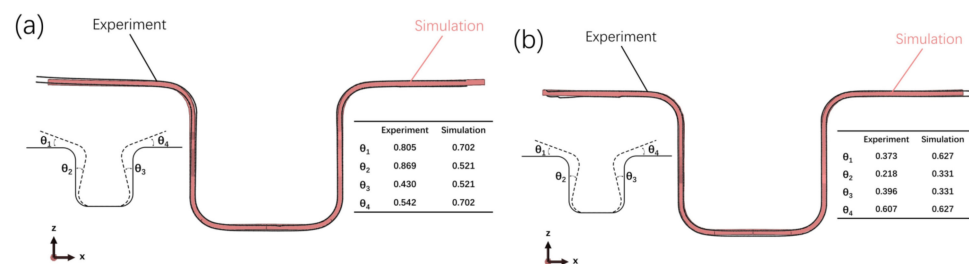


Figure 27. Comparison of the springback between numerical simulation of the U-shaped part and the blank used in the experiment. (a) TPP-S; (b) TPP-F.

8. Conclusions

In this paper, a 38MnB5Nb constitutive model considering the primary cooling temperature is proposed under the framework of a new tailored properties hot forming by partition cooling. The influence of different organization fields formed by partition cooling and tempering processes on the parameters of the unified viscoplastic constitutive model and the material parameters are determined by the optimization method based on a genetic algorithm. Considering the uneven temperature field generated by the partition cooling process, IHCP was able to obtain the relationship between the interfacial heat transfer coefficient and different cooling conditions in the partition cooling process. The established constitutive model and the interfacial heat transfer coefficient obtained from the inverse heat transfer method are applied to the commercial ABAQUS 2020/Explicit software and a numerical model for partition-cooling tailored properties hot-formed U-shaped parts is developed. The measurements of the thickness of the cross-section and the spring-back angles have verified that the numerical model is in good agreement with the experimental results.

Author Contributions: Conceptualization, X.L. (Xiao Liang), X.L. (Xianjun Li) and H.X.; methodology, X.L. (Xiao Liang), Z.T. and Y.T.; software, X.L. (Xiao Liang), Y.S. and Y.B.; validation, X.L. (Xiao Liang), X.L. (Xiyue Lin), P.L. and J.H.; formal analysis, X.L. (Xiao Liang); investigation, J.H.; resources, D.W., Y.S., Y.B., C.J. and X.L. (Xianjun Li); data curation, X.L. (Xiao Liang), Y.T. and X.L. (Xiyue Lin); writing—original draft preparation, X.L. (Xiao Liang) and X.L. (Xiyue Lin); writing—review and editing, X.L. (Xianjun Li), P.L., D.W., Y.S., Z.T., C.J., Y.B. and H.X.; visualization, X.L. (Xiao Liang); supervision, D.W.; project administration, J.H. and P.L.; funding acquisition, X.L. (Xianjun Li), D.W., C.J. and Y.B. All authors have read and agreed to the published version of the manuscript.

Funding: This research was funded by National Science and Technology Major Project of China, grant number 2018ZX04023002. National Science and Technology Major Project of China, grant number 2018ZX04044001, and China National Key R&D Program, grant number 2017YFB0701804.

Institutional Review Board Statement: Not applicable.

Informed Consent Statement: Not applicable.

Data Availability Statement: Not applicable.

Acknowledgments: Thanks to Ding, Y. and Yang, J. for their contributions to the proofreading of this article. Thanks to Ma, W.Y. for providing answers to encountered in establishing the constitutive model. Thanks to USTB and USTC for helping with the numerical simulation software. Thanks to Chen, W. for her help in the translation of the paper.

Conflicts of Interest: The authors declare no conflict of interest.

References

1. Nakagawa, Y.; Mori, K.; Suzuki, Y.; Shimizu, Y. Tailored Tempering without Die Heating in Hot Stamping of Ultra-High Strength Steel Parts. *Mater. Des.* **2020**, *192*, 108704. [[CrossRef](#)]
2. Nakagawa, Y.; Mori, K.; Maeno, T. Springback-Free Mechanism in Hot Stamping of Ultra-High-Strength Steel Parts and Deformation Behaviour and Quenchability for Thin Sheet. *Int. J. Adv. Manuf. Technol.* **2018**, *95*, 459–467. [[CrossRef](#)]
3. Eller, T.K.; Greve, L.; Andres, M.T.; Medricky, M.; Hatscher, A.; Meinders, V.T.; van den Boogaard, A.H. Plasticity and Fracture Modeling of Quench-Hardenable Boron Steel with Tailored Properties. *J. Mater. Process. Technol.* **2014**, *214*, 1211–1227. [[CrossRef](#)]

4. Tajul, L.; Maeno, T.; Kinoshita, T.; Mori, K. Successive Forging of Tailored Blank Having Thickness Distribution for Hot Stamping. *Int. J. Adv. Manuf. Technol.* **2017**, *89*, 3731–3739. [[CrossRef](#)]
5. Maeno, T.; Mori, K.-I.; Fujimoto, M. Improvements in Productivity and Formability by Water and Die Quenching in Hot Stamping of Ultra-High Strength Steel Parts. *CIRP Ann.* **2015**, *64*, 281–284. [[CrossRef](#)]
6. Jonsén, P.; Svanberg, A.; Ramirez, G.; Casellas, D.; Hernández, R.; Marth, S.; Häggblad, H.-Å.; Oldenburg, M. *A Novel Method for Modelling of Cold Cutting of Microstructurally Tailored Hot Formed Components*; Wissenschaftliche Scripten: Auerbach, Germany, 2019; pp. 645–652.
7. Lee, M.S.; Moon, J.H.; Kang, C.G. Investigation of Formability and Surface Micro-Crack in Hot Deep Drawing by Using Laser-Welded Blank of Al-Si and Zn-Coated Boron Steel. *Proc. Inst. Mech. Eng. Part B J. Eng. Manuf.* **2014**, *228*, 540–552. [[CrossRef](#)]
8. Lamprecht, K.; Geiger, M. Experimental and Numerical Investigation of the Formability of Laser Welded Patchwork Blanks. *Adv. Mater. Res.* **2005**, *6–8*, 689–696. [[CrossRef](#)]
9. Kim, J.H.; Ko, D.H.; Seo, P.G.; Kim, B.M. Limits Considering the Deformation Characteristics of Tailor Rolled Blank during Hot Stamping. *Trans. Mater. Process.* **2014**, *23*, 351–356. [[CrossRef](#)]
10. Merklein, M.; Wieland, M.; Lechner, M.; Bruschi, S.; Ghiotti, A. Hot Stamping of Boron Steel Sheets with Tailored Properties: A Review. *J. Mater. Process. Technol.* **2016**, *228*, 11–24. [[CrossRef](#)]
11. Landgrebe, D.; Putz, M.; Schieck, F.; Sterzing, A.; Rennau, A. Towards Efficient, Interconnected and Flexible Value Chains—Examples and Innovations from Research on Production Technologies. In Proceedings of the 5th International Conference on Accuracy in Forming Technology, Chemnitz, Germany, 10–11 November 2015; pp. 10–11.
12. Mori, K.; Maeno, T.; Mongkolkaji, K. Tailored Die Quenching of Steel Parts Having Strength Distribution Using Bypass Resistance Heating in Hot Stamping. *J. Mater. Process. Technol.* **2013**, *213*, 508–514. [[CrossRef](#)]
13. Maikranz-Valentin, M.; Weidig, U.; Schoof, U.; Becker, H.-H.; Steinhoff, K. Components with Optimised Properties Due to Advanced Thermo-Mechanical Process Strategies in Hot Sheet Metal Forming. *Steel Res. Int.* **2008**, *79*, 92–97. [[CrossRef](#)]
14. Mori, K.; Okuda, Y. Tailor Die Quenching in Hot Stamping for Producing Ultra-High Strength Steel Formed Parts Having Strength Distribution. *CIRP Ann.* **2010**, *59*, 291–294. [[CrossRef](#)]
15. Behrens, B.-A.; Bouguecha, A.; Gaebel, C.M.; Moritz, J.; Schrödter, J. Hot Stamping of Load Adjusted Structural Parts. *Procedia Eng.* **2014**, *81*, 1756–1761. [[CrossRef](#)]
16. Tang, B.T.; Wang, Q.L.; Bruschi, S.; Ghiotti, A.; Bariani, P.F. Influence of Temperature and Deformation on Phase Transformation and Vickers Hardness in Tailored Tempering Process: Numerical and Experimental Verifications. *J. Manuf. Sci. Eng.* **2014**, *136*, 051018. [[CrossRef](#)]
17. Bardelcik, A.; Vowles, C.J.; Worswick, M.J. A Mechanical, Microstructural, and Damage Study of Various Tailor Hot Stamped Material Conditions Consisting of Martensite, Bainite, Ferrite, and Pearlite. *Metall. Mater. Trans. A* **2018**, *49*, 1102–1120. [[CrossRef](#)]
18. Omer, K.; ten Kortenaar, L.; Butcher, C.; Worswick, M.; Malcolm, S.; Detwiler, D. Testing of a Hot Stamped Axial Crush Member with Tailored Properties—Experiments and Models. *Int. J. Impact. Eng.* **2017**, *103*, 12–28. [[CrossRef](#)]
19. Omer, K.; George, R.; Bardelcik, A.; Worswick, M.; Malcolm, S.; Detwiler, D. Development of a Hot Stamped Channel Section with Axially Tailored Properties—Experiments and Models. *Int. J. Mater. Form.* **2018**, *11*, 149–164. [[CrossRef](#)]
20. Múnera, D.D.; Pic, A.; Abou-Khalil, D.; Shmit, F.; Pinard, F. Innovative Press Hardened Steel Based Laser Welded Blanks Solutions for Weight Savings and Crash Safety Improvements. *SAE Int. J. Mater. Manuf.* **2009**, *1*, 472–479. [[CrossRef](#)]
21. Tang, B.; Wang, Q.; Wei, Z.; Meng, X.; Yuan, Z. FE Simulation Models for Hot Stamping an Automobile Component with Tailor-Welded High-Strength Steels. *J. Mater. Eng. Perform.* **2016**, *25*, 1709–1721. [[CrossRef](#)]
22. Billur, E.; Bošković, V. Tailored Properties. In *Hot Stamping of Ultra High-Strength Steels: From a Technological and Business Perspective*; Billur, E., Ed.; Springer International Publishing: Cham, Switzerland, 2019; pp. 157–190. ISBN 978-3-319-98870-2.
23. Lei, C.; Xing, Z.; Xu, W.; Wu, Y.; Li, Y.; Shan, D. Flow Behavior of High Strength Steel TRB at Elevated Temperature. *Cailiao Kexue Gongyi Mater. Sci. Technol.* **2015**, *23*, 66–70. [[CrossRef](#)]
24. Ou, H.; Yang, Y.; Hu, M.; Li, G.; Cui, J. Forming Study on a Tailor Rolled Blank (TRB) Structure-Formability Evaluation and Model Verification. *J. Manuf. Process.* **2019**, *44*, 397–407. [[CrossRef](#)]
25. Wilsius, J.; Tavernier, B.; Abou-Khalil, D. Experimental and Numerical Investigation of Various Hot Stamped B-Pillar Concepts Based on Usibor® 1500P. In Proceedings of the 3rd International Conference on Hot Sheet Metal Forming of High-Performance Steel, Kassel, Germany, 13–16 June 2011; pp. 427–435.
26. Mori, K. Smart Hot Stamping of Ultra-High Strength Steel Parts. *Trans. Nonferrous Met. Soc. China* **2012**, *22*, s496–s503. [[CrossRef](#)]
27. Mu, Y.; Zhou, J.; Wang, B.; Wang, Q.; Ghiotti, A.; Bruschi, S. Numerical Simulation of Hot Stamping by Partition Heating Based on Advanced Constitutive Modelling of 22MnB5 Behaviour. *Finite Elem. Anal. Des.* **2018**, *147*, 34–44. [[CrossRef](#)]
28. Feuser, P.; Schweiker, T.; Merklein, M. Partially Hot-Formed Parts from 22MnB5-Process Window, Material Characteristics and Component Test Results. In Proceedings of the 10th International Conference on Technology of Plasticity, Aachen, Germany, 25–30 September 2011; pp. 25–30.
29. Casas, B.; Latre, D.; Rodriguez, N.; Valls, I. Tailor Made Tool Materials for the Present and Upcoming Tooling Solutions in Hot Sheet Metal Forming. In Proceedings of the 1st International Conference on Hot Sheet Metal Forming of High-Performance steel, Kassel, Germany, 22–24 October 2008; pp. 23–35.

30. Kolleck, R.; Veit, R. *Möglichkeiten Zur Lokalen Beeinflussung Der Bauteilfestigkeit Beim Presshärten*; Erlangen Workshop Warmblechumformung: Erlangen, Germany, 2008; pp. 65–72.
31. Zimmermann, F.; SpÖer, J.; Volk, W. Partial Tempering of Press Hardened Car Body Parts by a Premixed Oxygen-Methane Flame Jet. In Proceedings of the 4th International Conference on Hot Sheet Metal Forming of High-Performance Steel, Luleå, Sweden, 9–12 June 2013; pp. 9–10.
32. Xiang, G.Z.; Zhang, Y.S.; Wang, Z.J. A New Technology of Hot Stamping Ultra-high Strength Automobile selective Cooling. *Hot Work. Technol.* **2013**, *42*, 108–113. [[CrossRef](#)]
33. Zhou, J. Study on Hot Stamping and Damage Evolution of Boron Steel by Thermal Simulating Experiment Modelling and Simulation. Ph.D. Thesis, University of Science and Technology, Beijing, China, 2017.
34. Li, H.; He, L.; Zhao, G.; Zhang, L. Constitutive Relationships of Hot Stamping Boron Steel B1500HS Based on the Modified Arrhenius and Johnson–Cook Model. *Mater. Sci. Eng. A* **2013**, *580*, 330–348. [[CrossRef](#)]
35. Cao, S.F.; Zhang, L.Q.; Guo, P.C.; Li, L.X. Study on Hot Deformation Behavior and Flow Stress Constitutive Model of 22MnB5 at High Temperature. *China Mech. Eng.* **2014**, *25*, 1256–1261.
36. Lin, J.; Liu, Y. A Set of Unified Constitutive Equations for Modelling Microstructure Evolution in Hot Deformation. *J. Mater. Process. Technol.* **2003**, *143–144*, 281–285. [[CrossRef](#)]
37. Lin, J.; Liu, Y.; Farrugia, D.C.J.; Zhou, M. Development of Dislocation-Based Unified Material Model for Simulating Microstructure Evolution in Multipass Hot Rolling. *Philos. Mag.* **2005**, *85*, 1967–1987. [[CrossRef](#)]
38. Politis, N.; Politis, D.J.; Davies, C.M.; Lin, J. A Method of Determining Unified Viscoplastic Constitutive Equations for Hot Forging Simulations. *Key Eng. Mater.* **2016**, *716*, 251–261. [[CrossRef](#)]
39. Zhong, H.; Wang, Z.; Gan, J.; Wang, X.; Yang, Y.; He, J.; Wei, T.; Qin, X. Numerical Simulation of Martensitic Transformation Plasticity of 42CrMo Steel Based on Spot Continual Induction Hardening Model. *Surf. Coat. Technol.* **2020**, *385*, 125428. [[CrossRef](#)]
40. Alberg, H.; Berglund, D. Comparison of Plastic, Viscoplastic, and Creep Models When Modelling Welding and Stress Relief Heat Treatment. *Comput. Methods Appl. Mech. Eng.* **2003**, *192*, 5189–5208. [[CrossRef](#)]
41. Cai, J. Modelling of Phase Transformation in Hot Stamping of Boron Steel. Ph.D. Thesis, Imperial College London, London, UK, 2011.
42. Tang, B.T.; Bruschi, S.; Ghiotti, A.; Bariani, P.F. Numerical Modelling of the Tailored Tempering Process Applied to 22MnB5 Sheets. *Finite Elem. Anal. Des.* **2014**, *81*, 69–81. [[CrossRef](#)]
43. Garson, G.D. *Correlation*, 2013rd ed.; Statistical Associates Publishers: Asheboro, NC, USA, 2012; pp. 154–196.
44. Mirsepahi, A. An Intelligent Approach to Inverse Heat Transfer Analysis of Irradiative Enclosures. Ph.D. Thesis, University of Adelaide, Adelaide, Australia, 2017.
45. Karnal, M. High Temperature Measurements at the Internal Nozzle Wall of the Zephyr. Master’s Thesis, Luleå University of Technology, Luleå, Sweden, 2014.
46. Liu, H.S.; Xing, Z.W.; Bao, J.; Song, B.Y. Investigation of the Hot-Stamping Process for Advanced High-Strength Steel Sheet by Numerical Simulation. *J. Mater. Eng. Perform.* **2010**, *19*, 325–334. [[CrossRef](#)]
47. Warlimont, H. *Metal Forming Data of Ferrous Alloys—Deformation Behaviour*; Springer Berlin Heidelberg: Berlin, Germany, 2009; pp. 15–278.
48. Turetta, A.; Bruschi, S.; Ghiotti, A. Investigation of 22MnB5 Formability in Hot Stamping Operations. *J. Mater. Processing Technol.* **2006**, *177*, 396–400. [[CrossRef](#)]
49. Abdollahpoor, A.; Chen, X.; Pereira, M.P.; Xiao, N.; Rolfe, B.F. Sensitivity of the Final Properties of Tailored Hot Stamping Components to the Process and Material Parameters. *J. Mater. Process. Technol.* **2016**, *228*, 125–136. [[CrossRef](#)]
50. Shapiro, A.B. Using LS-Dyna for Hot Stamping. In Proceedings of the 7th European LS-DYNA Users Conference, Salzburg, Austria, 14–15 May 2009.
51. Naderi, M. Hot Stamping of Ultra High Strength Steels. Ph.D. Thesis, Amirkabir University of Technology, Tehran, Iran, 2007.